Applications of 3D printing in small animal magnetic resonance imaging

John C. Nouls
Rohan S. Virgincar
Alexander G. Culbert
Nathann Morand
Dana W. Bobbert
Anne D. Yoder
Robert S. Schopler
Mustafa R. Bashir
Alexandra Badea
Ute Hochgeschwender
Bastiaan Driehuys

SPIE.

Applications of 3D printing in small animal magnetic resonance imaging

John C. Nouls,[a,*] Rohan S. Virgincar,[b] Alexander G. Culbert,[b] Nathann Morand,[c] Dana W. Bobbert,[d] Anne D. Yoder,[e,f] Robert S. Schopler,[f] Mustafa R. Bashir,[a] Alexandra Badea,[a] Ute Hochgeschwender,[g] and Bastiaan Driehuys[a,b]

[a]Duke University Medical Center, Department of Radiology, Durham, North Carolina, United States
[b]Duke University, Department of Biomedical Engineering, Durham, North Carolina, United States
[c]Ecole des Métiers, Fribourg, Switzerland
[d]Duke University, Office of Information Technology, Durham, North Carolina, United States
[e]Duke University, Department of Biology, Durham, North Carolina, United States
[f]Duke University, Lemur Center, Durham, North Carolina, United States
[g]Central Michigan University, College of Medicine, Mount Pleasant, Michigan, United States

Abstract. Three-dimensional (3D) printing has significantly impacted the quality, efficiency, and reproducibility of preclinical magnetic resonance imaging. It has vastly expanded the ability to produce MR-compatible parts that readily permit customization of animal handling, achieve consistent positioning of anatomy and RF coils promptly, and accelerate throughput. It permits the rapid and cost-effective creation of parts customized to a specific imaging study, animal species, animal weight, or even one unique animal, not routinely used in preclinical research. We illustrate the power of this technology by describing five preclinical studies and specific solutions enabled by different 3D printing processes and materials. We describe fixtures, assemblies, and devices that were created to ensure the safety of anesthetized lemurs during an MR examination of their brain or to facilitate localized, contrast-enhanced measurements of white blood cell concentration in a mouse model of pancreatitis. We illustrate expansive use of 3D printing to build a customized birdcage coil and components of a ventilator to enable imaging of pulmonary gas exchange in rats using hyperpolarized ^{129}Xe. Finally, we present applications of 3D printing to create high-quality, dual RF coils to accelerate brain connectivity mapping in mouse brain specimens and to increase the throughput of brain tumor examinations in a mouse model of pituitary adenoma. © 2019 Society of Photo-Optical Instrumentation Engineers (SPIE) [DOI: 10.1117/1.JMI.6.2.021605]

Keywords: additive manufacturing; 3D printing; preclinical; animal; magnetic resonance imaging.

Paper 18205SSRRR received Sep. 14, 2018; accepted for publication Apr. 15, 2019; published online May 15, 2019.

1 Introduction

The ability to rapidly and cost-effectively produce three-dimensional (3D) parts from digital models by additive manufacturing[1] continues to find new applications in medicine[2–5] and gain broader adoption. For example, medical imaging data derived from a specific patient can be used to create anatomically exact replicas of impaired organs;[6] such replicas have been proven valuable for surgery planning prior to complex interventions in cardiothoracic, vascular,[7–10] reconstructive surgery,[11,12] and surgical oncology.[13] Moreover, 3D printing has been used to individualize anatomically conforming prostheses and implants or to produce surgical instruments and guides.[14,15] This technology has also been proven transformative in tissue engineering and regenerative medicine.[16–19]

Furthermore, 3D printing has been used in precision medicine to combine personalized pharmacologic agents into drug-delivery substrates.[20]

While the opportunities for 3D printing within clinical medicine are vast, this technology has had an equally positive impact on advancing preclinical research[21–23] and imaging.[22,24–40] Additive manufacturing permits the creation and customization of assemblies that facilitate the handling of an uncooperative animal, the control of anesthesia, the positioning of organs of interest within the imaging equipment, and the optimization of data acquisition.[25] Among the different imaging modalities employed in preclinical research, those challenges are often compounded in the context of small-animal magnetic resonance imaging (MRI). This is attributable to the exceptionally constrained space in the magnet bore, restricted access, MR-compatibility requirements, and the vast differences of scale between the animal and the magnet.

Here, we present several applications illustrating the value of additive manufacturing for small-animal MRI research. We summarize the experimental requirements and present specific solutions enabled by 3D printing to enhance the safety of lemurs placed under anesthesia during an MR examination of their brain or to facilitate measurements of white blood cell concentration in a mouse model of pancreatitis. We further illustrate the benefits of 3D printing in an experiment of pulmonary gas-exchange imaging using hyperpolarized (HP) ^{129}Xe in rats. Multiple components are 3D printed to ventilate rats mechanically and to build a customized birdcage coil. Finally, we present applications of 3D printing to create atypical radio frequency (RF) coils for brain connectivity mapping in mouse brain specimens and to increase the throughput of brain tumor examinations in a mouse model of pituitary adenoma.

While these applications demonstrate the potential of 3D printing for specific small-animal MRI projects, they only partially reflect the diversity and significance of ongoing research

---

in the field. Thus, wherever possible we have also included references to related work for readers interested in gaining a wider perspective.

2 Overview of Preclinical MRI

To appreciate the benefits of 3D printing for preclinical MRI, it is important to understand the principal challenges facing this discipline. One such challenge lies in the inherently smaller voxel volumes that must be imaged in preclinical versus clinical MRI. That is, to maintain the same relative anatomical definition between a 1400-cm³ human brain and, for example, the 1.9-cm³ brain of a lemur,[41] the voxel volume must be decreased by a factor of ∼700. This translates into a pixel spanning over an anatomical extent nine times smaller in each spatial direction. Obtaining such high resolution requires overcoming the SNR deficit inherent in preclinical MRI through several means.

SNR gains are primarily achieved by operating preclinical scanners at higher field. For example, relative to a typical 1.5 T clinical field strength, preclinical imaging at 9.4 T enhances SNR by a factor ranging between 6 and 40, depending on the origin of the imaging noise.[42,43] Other SNR gains can be obtained from high-performance gradient systems and electronics or by lengthening the acquisition time.[43] To improve SNR further, preclinical RF coils are usually designed to surround the organ of interest very closely. Additional SNR gains have been achieved by cooling the RF coil and preamplifiers cryogenically.[24,44] These SNR enhancement techniques can be combined differently; however, preclinical MR acquisitions lasting tens of minutes to an hour are often required to reverse-translate minute-long timescales in human MRI.

During the relatively long preclinical MR acquisition, motion poses significant challenges.[45,46] At an in-plane resolution of a few hundred micrometers, imaging can be severely degraded by minimal positional changes of the animal and by cardiac or respiratory motion.[25,26,47,48] While cyclical motion can be addressed by gating, preclinical magnets rely on several fixtures to safely restrain the animal within the gradient coils, to hold in place the RF coil and the organ of interest, and to prevent any movement caused by vibrations associated with the switching of gradient coils during imaging. These coil-specific and organ-specific fixtures restrain motion physically and are often used in combination with chemical restraint via anesthesia.

In small-animal MRI, anesthesia is usually administered by inhalant agents, through a nose cone attached to an animal support bed at the center of the magnet. Alternatively, injectable anesthetics may be used, and if needed, maintenance doses can be administered remotely through lines of tubing and transcutaneous catheters without moving the animal out of the bore. Anesthetic depth can be assessed by monitoring several physiological functions, including the spontaneous breathing rate, heart rate, or blood oxygenation. Notably, anesthetics also have the side effect of depressing the animal's ability to self-regulate body temperature,[49] which, coupled with fluctuations of the bore temperature driven by the gradient duty cycle, requires extraneous regulation of animal temperature. This extraneous control is commonly achieved by monitoring body temperature, and flowing temperature-controlled air within the bore, or circulating temperature-regulated water through pads in contact with the animal.

In the following sections, we illustrate these principles in more detail with application-specific examples from our imaging center.

3 Application-Specific Optimization

3.1 Brain Imaging in Lemurs

To illustrate one way in which 3D printing facilitated a preclinical MRI study, we describe a bed that has been developed specifically for brain imaging in the mouse lemur (*Microcebus murinus*) and fat-tail lemur (*Cheirogaleus medius*).

The experimental requirements were twofold. First, strong T_2 contrast had to be achieved in the lemur brain at high field, on a 7-T preclinical scanner (Bruker BioSpec 70/20 USR, Billerica, Massachusetts). The imaging sequence selected
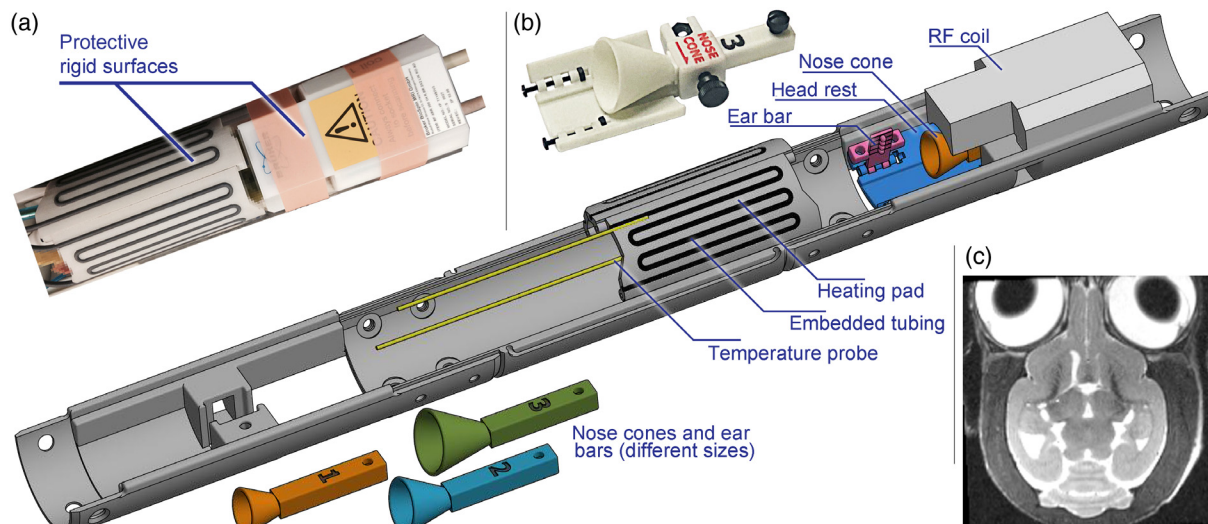

Fig. 1 (a) Picture of the lemur bed, designed to fully surround the lemur body with protective, rigid surfaces. (b) Model used for selective laser sintering. The rigid heating pad features complex voids, which permit the integration of flexible tubing and two temperature probes into the 3D-printed material. The head rest is produced with several polygonal voids to embed hexagonal nuts and miniaturized adjustment mechanisms. In addition, multiple nose cones and ear bars of various sizes could be 3D printed. (c) MR image of the brain of a mouse lemur, acquired in 28 min by a multislice fast spin echo acquisition.

for imaging was sensitive to motion, which made it necessary to prevent head movement throughout multiple respiratory and cardiac cycles during MR acquisition. However, the widely differing facial anatomy of these lemurs precluded the use of commercial immobilization fixtures compatible with rodents only. Thus, fixtures such as the nose cone and ear bars required a redesign to conform to the lemur anatomy. Second, exceptional precautions during animal handling were required to minimize the risk of injury or death, as lemurs are overly rare primates belonging to an endangered and protected species.

To meet these requirements, a customized lemur bed was developed, as shown in Fig. 1(a). The device was designed with rigid surfaces to enshroud the entire lemur body and thereby minimize the risk of accidental trauma during animal handling and transport. The surface-receive RF coil was also used as a protective structure for the lemur head. The coil was securely held in place by lateral guides built into the bed, and an adjustable head rest could be raised to ensure the proper positioning of the lemur skull within the coil. To control body temperature, warm water was circulated through flexible tubing inserted into two rigid heating pads. To minimize the risk of accidental burns, skin and water temperature were monitored by integrating into the heating pads two MR-compatible fiber-optic temperature probes (T1, Rugged Monitoring, Québec City, Canada). The bed was 3D printed by selective laser sintering (3D Systems, Rock Hill, South Carolina), using an engineered glass-filled polymer (DuraForm GF, 3D Systems). This process and material were selected for several reasons: first, the build volume (76 cm × 51 cm × 51 cm) within the selective laser sintering printer was sufficiently large to produce the 65-cm long, 7.2-cm-diameter bed. Second, protrusions or voids as small as 0.75 mm in size could be reliably created, which enabled the integration of miniaturized adjustment mechanisms into the bed (screws and hexagonal nut size M2 or larger). Last, the durable, impact- and heat-resistant polymer could withstand warm water reaching 60°C without deformation. One of the benefits of additive manufacturing was that nose cones of various sizes could be created cost-effectively so that the one best conforming to the lemur face could be used to administer inhalant anesthetics (isoflurane, Forane, Baxter, Deerfield, Illinois), in a fashion similar to Mundinano et al.'s study.[50] Similarly, multiple ear bars of various shapes were also manufactured and the best fitting ones were selected to minimize the risk of trauma. Figure 1(b) shows the principal components of the bed, and an example of the MR images that were acquired.

3.2 Pancreas T_2 Relaxometry in Mice

Optimal imaging of animals of different species and sizes requires a variety of readily interchangeable beds. Such modifiable beds can be created quickly by 3D printing and connected to a distribution dock that guides various lines for sensors, anesthesia, and physiological support. In such a modular system, these lines could remain permanently connected to their associated equipment outside the bore so that different beds may be readily exchanged. Figure 2(a) shows such a universal distribution dock, attached to a customizable bed at the center of the magnet. The dock contains several segments so that beds of various lengths could be centered in the magnet. In this application, the dimensions of the bed are tailored to facilitate MR measurements of white blood cell concentration in the mouse pancreas.
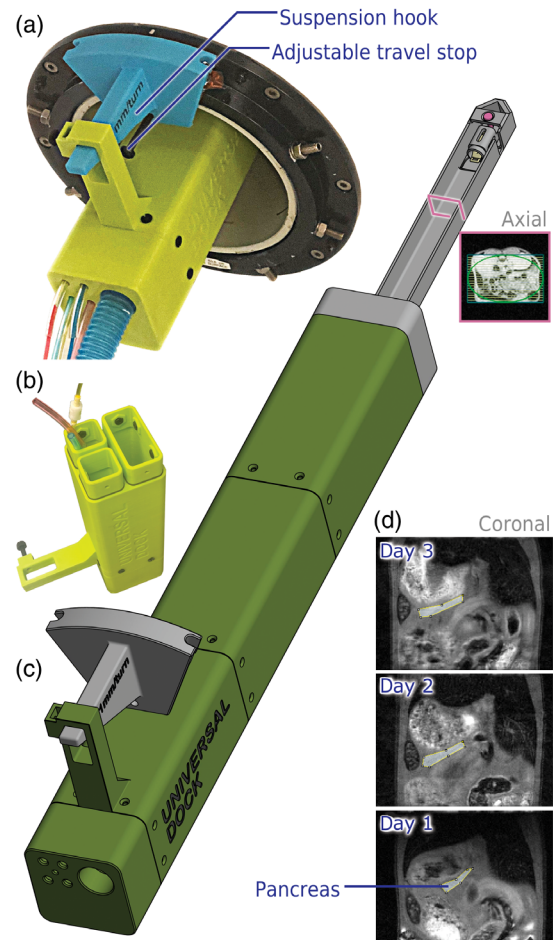

Fig. 2 (a) Picture of the universal dock suspended at the opening of the magnet bore. The cross section (a square 85 mm in size, with rounded corners of 11-mm radius) was 3D-printed so that the dock self-centers into the 112-mm-diameter bore of the gradient coils. At the magnet opening, a flat hook enables adjustments of the position of the dock-and-bed assembly along the z-direction. The hook also features an adjustable travel stop to repeatedly position the dock at the same location in the magnet. (b) Picture of an internal connection of the dock. (c) The 3D model of the dock attached to a bed custom-made for a relaxivity measurement in the mouse abdomen. The bed is built with a rectangular cross section matching the imaging field of view. The picture insert shows a MR image of the mouse abdomen held within the imaging volume of the MR measurement. (d) Coronal images of the same mouse, imaged on three different days, illustrating the repeatability of pancreas positioning (outlined) within the imaging volume.

This study investigated a mouse model of abdominal inflammation causing acute pancreatitis. Prior to imaging, a superparamagnetic iron-oxide particle (Ferumoxytol, Feraheme, Amag Pharmaceuticals, Waltham, Massachusetts) was injected intravenously, causing the particles to be internalized in phagocytic white blood cells.[51] Cells migrating to the site of inflammation caused a local shortening of T_2 measured by MR relaxometry; this principle permitted the assessment of macrophage abundance in pancreatic tissue and thereby gauged the severity of pancreatitis.

Such relaxometry measurements could achieve adequate temporal and spatial resolutions in an imaging volume limited to 16 coronal slices, 1-mm thick, encoding a 26 × 28 mm field of view. Because the pancreas is inconspicuous in localizer

scans, the position of the imaging volume could not be adjusted easily prior to initiating the relaxometry measurement. Rather, to expedite imaging, an inverse approach was taken, which required the abdomen to be placed consistently within the pre-defined imaging volume. To achieve this, the bed was designed with a rectangular cross section matching the imaging volume, which would center the mouse abdomen within the volume RF coil (T9988V3, Bruker, Billerica, Massachusetts). The bed and the universal dock were 3D printed by fused filament fabrication (Ultimaker 2+, at the Duke Co-Lab, Durham, North Carolina) on account of the low cost of that process and using polylactide, a relatively inexpensive MR-compatible polymer.[25] The customized bed facilitated both the identification of the pancreas in different animals and following it longitudinally in the same animal. Figure 2(c) illustrates the reproducibility of pancreas positioning, by showing a relaxivity measurement repeated three times in the same animal 24-h apart.

3.3 Imaging Pulmonary Gas Exchange with Hyperpolarized ^{129}Xe in Rats

HP ^{129}Xe MRI is a technique that images the distribution of ^{129}Xe gas in pulmonary airspaces and tissues, and thereby enables the regional assessment of ventilation and gas exchange. The advancement of ^{129}Xe imaging in the clinic[52–54] has driven an interest for a reverse translation in the preclinical environment to validate new applications. However, small-animal ^{129}Xe imaging is challenging because the depiction of heterogeneous pulmonary diseases requires 3D encoding at sub-millimeter spatial resolution. This resolution has been recently attained isotropically in rats at 7 T, using a custom-built mechanical ventilator[55] compatible with HP xenon. 3D printing has been instrumental in the manufacturing of gas-handling components compatible with HP xenon, the construction of a birdcage coil, and the production of a bed for intubated rats.

3D printing permits the production of miniaturized gas-mixing manifolds made from materials compatible with HP gas.[56] Oxygen, xenon, and exhaled gas are transported separately by different lines of tubing to mechanically ventilate rodents for ^{129}Xe imaging. Figure 3(a) shows the intubated rodent at the magnet center, the separate gas lines, and the ventilator at the opening of the bore. The gas lines are merged within a mixing manifold, which is connected to the intubation catheter in the trachea. Figure 3(b) shows the gas manifold and its dead volume, which are minimized to ensure that the supply of oxygen to the rodent lungs remains adequate. The gas manifold is composed of two halves, 3D printed by fused filament fabrication (Ultimaker 3, at the Duke Co-Lab, Durham, North Carolina) from HP-gas-compatible polylactide, as shown in Fig. 3(c). To achieve sufficient detail, each half is built using a 0.25-mm diameter extrusion nozzle and 0.1-mm-thick layers. The two halves are attached together by ethyl-cyanoacrylate glue (Loctite 401, Henkel, Rocky Hill, Connecticut) and coated with epoxy (XTC-3D, Smooth-On Inc., Macungie, Pennsylvania) to create a gas-tight connector.

The administration of HP xenon to the anesthetized rodent is particularly challenging. The HP state of the gas is susceptible to unwanted relaxation, caused by interactions of HP gas with paramagnetic or ferromagnetic impurities in materials that store or transport the gas. Hence, HP gas was stored in a perfluoro-polymer dose bag (Polarean Inc., Durham, North Carolina), devoid of these impurities. To deliver this gas to the animal, the dose bag was pressurized to ~0.2 bar within a pressure
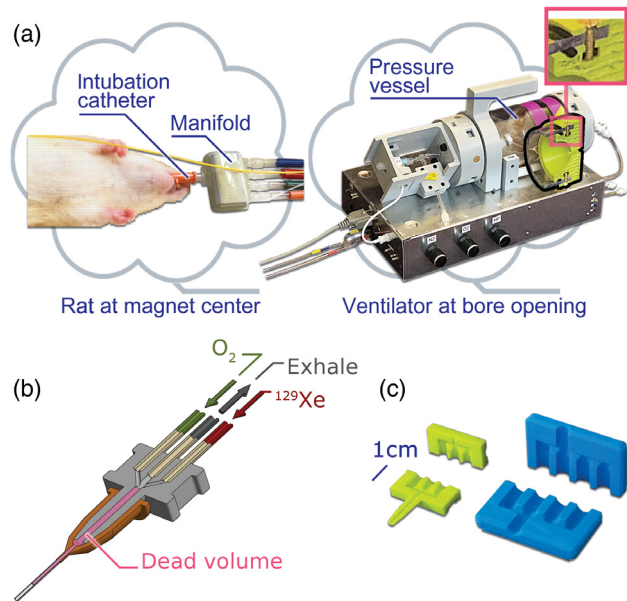

Fig. 3 (a) Oxygen, xenon, and exhaled gas are transported between the ventilator and the intubated rat by separate lines, merging into a miniaturized gas manifold. To illustrate the construction of the pressure vessel supplying ^{129}Xe gas, an endcap is cut in half (outlined in black, on the right). The magnified picture insert shows the smooth barrier of full-density PLA providing a pressure-tight barrier, and the internal cross-hatch pattern. (b) Schematic representation of the cross section of a gas manifold connected to the intubation catheter in the trachea. The minimized dead volume is indicated in pink. (c) To provide sufficient amounts of oxygen to a 200-g rat with a 2-mL tidal volume, the gas manifold (blue color, far right) is designed to limit the dead volume to <0.2 mL only and is built from two halves. A smaller manifold (green color, on the left) is made for smaller rats.

vessel, as shown in Fig. 3(a). Xenon was delivered to the animal through a nonmetallic, pneumatically actuated valve that was integrated into the pressure vessel, which relied on several o-rings to establish pressure-tight seals. Construction of this HP gas-delivery apparatus also benefitted from 3D printing to curtail fabrication cost. In particular, the endcaps of the pressure vessel were 3D printed by fused filament fabrication from stiff technical polylactide (tough PLA, Ultimaker, Geldermalsen, The Netherlands) to withstand pressure, in successive 0.1-mm-high layers to provide a smooth surface finish compatible with o-rings. The endcaps were printed with a 2-mm-thick outer shell of full-density PLA to create a barrier adequately pressure-tight, and the inner volume of the part was filled in a cross-hatch pattern with 35% PLA by volume to limit build time. The pressure vessel could withstand a pressure exceeding 1 bar.

For the same study, additive manufacturing was also used to create a custom ^{129}Xe volume RF transmit/receive coil. Figure 4 shows the birdcage coil assembly, also constructed from polylactide parts. An inner frame contained incision guides allowing a sheet of copper to be easily cut into the shape of a 16-leg, low-pass birdcage coil. The frame also included 16 wells, which facilitated the soldering of capacitors (800 B-series nonmagnetic, American Technical Ceramics, Huntington Station, New York). An outer casing, also 3D printed, was wrapped in copper to ground and shield the RF coil against extraneous RF noise.

The different frames contained geometrically complex voids, used to embed threaded nuts, screws, or other mechanisms
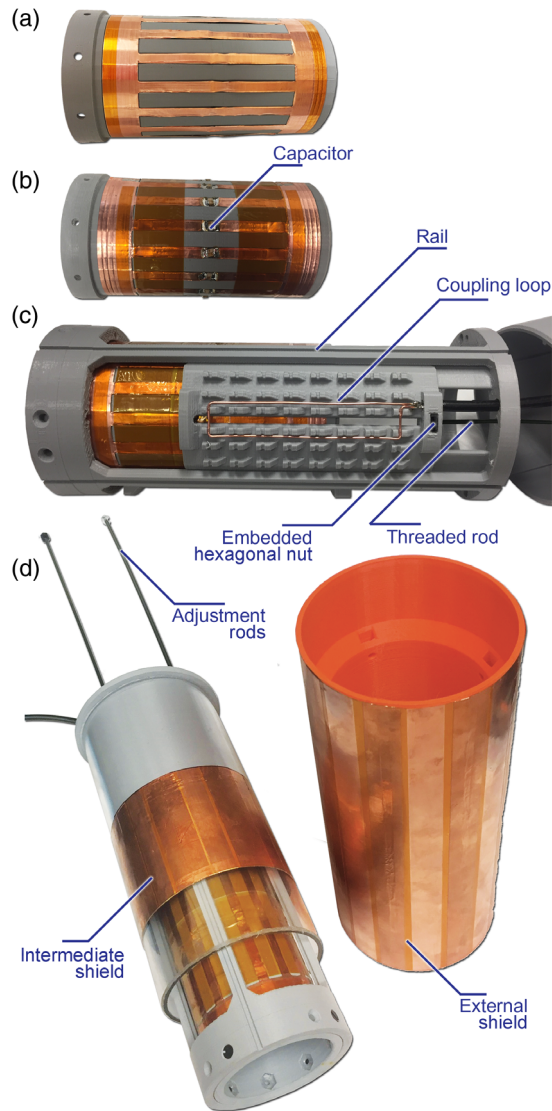
Fig. 4 (a) Fabrication of the birdcage coil, from a 0.12-mm-thick sheet of copper wrapped around the inner frame. Incision guides in the 3D-printed frame allowed the copper to be cut into the shape of a 16-leg, low-pass birdcage coil. (b) The 16 wells 3D printed in the frame facilitate the soldering of capacitors. (c) A plate could hold coupling loops of different sizes. Internal guiding rails, embedded polycarbonate nuts, and a vinyl-threaded rod could be used to translate the position of the loop and impedance match the coil. (d) An intermediate, floating, split shield could be moved to tune the resonant frequency of the coil.

adjusting the performance of the coil. For example, to adjust the impedance match of the coil or tune the resonant frequency, rods were integrated into rails that physically moved an intermediate shield or a coupling loop along the axis of the coil (Fig. 4). These rods could be reached from outside the bore, and made it possible to optimally tune and match the coil immediately prior to MR acquisition.

A bed was also customized and 3D printed for intubated, mechanically ventilated, 8-to-12-week-old Sprague-Dawley rats weighing 150 to 250 g. The bed positioned the lungs on magnet isocenter, as the 3D radial MR acquisitions commonly used in ^{129}Xe MRI did not permit field-of-view offsets. The bed integrated several sensors for monitoring physiology, which also allowed MR data acquisition to be synchronized with
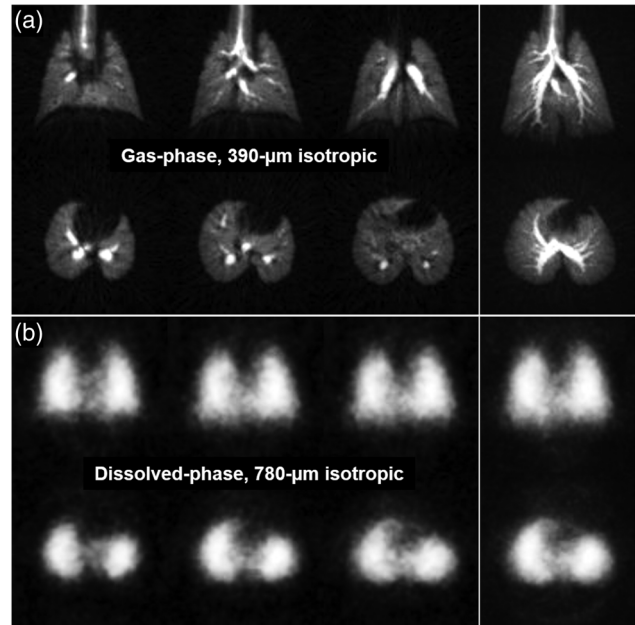

Fig. 5 (a) HP ^{129}Xe ventilation images at 7 T in a healthy rat, intubated and mechanically ventilated. Coronal views are shown on the top row, and axial views on the bottom row. Maximum-intensity projections are shown on the right. (b) Colocalized images of ^{129}Xe that is dissolved in lung tissue and blood.

the respiratory cycle. It contained an airway pressure transducer (Fujikura AG206-025k, Servoflo Corporation, Lexington, Massachusetts), three pediatric ECG pads (Ambu, Columbia, Maryland), and a rectal fiber optic thermometer. The bed included built-in fixtures to immobilize the lines carrying breathing gases and sensor signals relative to the trachea, and thus precluded accidental trauma during animal transport, such as extubation or ventilation interruption.

Figure 5 shows images of HP xenon in airspaces and dissolved in tissue, acquired in rats, to the best of our knowledge, for the first time at 7 T.

3.4 Diffusion Tensor Imaging in Mouse Brain Specimens

The 3D printers have reached a build resolution approaching ~0.01 mm and can use engineered plastics providing a rigidity comparable to machined polymers. A rigid 3D-printed frame, combined with thin and geometrically complex internal holders, enabled a low-cost and high-throughput application of diffusion tensor imaging (DTI) in mouse brain specimens.

The demonstration of a link between brain connectivity and psychiatric or neurological diseases has stimulated the development of brain connectivity mapping techniques in humans and in mouse models of human disease. The neural architecture can be measured by DTI, which enables high-resolution brain tractography, the establishment of a connectivity matrix, and connectomics. However, in mouse brain specimens, such experiments can require tens of hours of magnet time and can become prohibitively long.[57]

To increase throughput, a two-coil system was developed to scan two mouse brain specimens simultaneously. Each coil was shielded, placed off-isocenter along the axis of the magnet, and connected to a separate receiver circuit of a 7-T preclinical scanner (Bruker BioSpec 70/20 USR, Billerica, Massachusetts).

At 7 T, each coil examined a mouse brain specimen in a regime where MRI noise originated predominantly in the RF coil. This rendered SNR and throughput very sensitive to the coil quality factor,[57] which is a metric of the power dissipated in each coil.

An original, high-quality-factor RF coil was developed and its fixture was 3D printed twice. The fixture permitted a sheet of copper to be folded tightly around a mouse brain specimen, which formed an inductive loop followed by a two-plate capacitor. Figure 6(a) shows the mouse brain specimen in a holder, the sheet of copper, and the unusual RF coil. The capacitor was created from a central sheet of low-dielectric-loss sapphire, which was pressed between both ends of the copper sheet, as seen in Fig. 6(b). The capacitor was held together by rigid, sapphire-covered clamps, pressed together forcefully by a thick, sturdy outer frame. These parts were 3D printed by selective laser sintering, using a stiff engineered polymer (DuraForm GF, 3D Systems, tensile modulus 4068 MPa). This provided sufficient rigidity to avoid alterations of the capacitor geometry over the 11-h-long MR acquisition and changes of the RF coil resonant frequency. In contrast, the internal holders of the brain specimen and copper sheet were produced by stereolithography (Quickparts, 3D Systems) using a high-resolution polymer resin (High-Resolution Accura SL 7811, 3D Systems). This allowed the production of very detailed internal fixtures. For example, thin parts—only 0.25-mm thick—could be fabricated, and
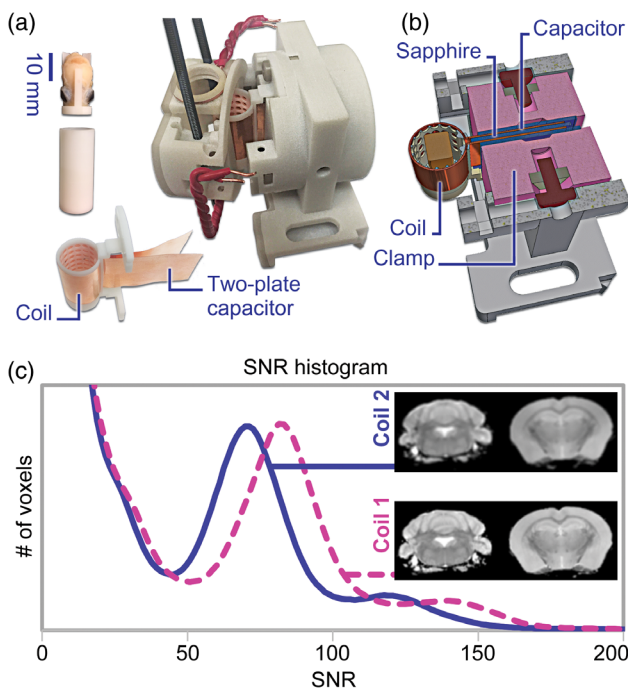

Fig. 6 (a) Mouse brain specimen and its container 3D printed by stereolithography to produce 0.25-mm-thick walls (left). The copper sheet forming the RF coil is wrapped around a 0.25-mm thick, perforated fixture (bottom). The rigid, thick outer assembly produced by selective laser sintering is opened to show the construction of the RF coil. The coil resonates at 300 MHz. Tuning of the resonant frequency is achieved by an internal mechanism that adjusted the position of a tuning loop, whereas impedance matching is accomplished by adjusting the position of an inductive loop coupled to the coil. (right) (b) Half view through the RF coil assembly. Sapphire-covered clamps forcefully press the two-plate capacitor around a central, 2-mm-thick dielectric sheet of sapphire. (c) The DTI images acquired show no artifacts, and the two coils exhibit similar SNR.
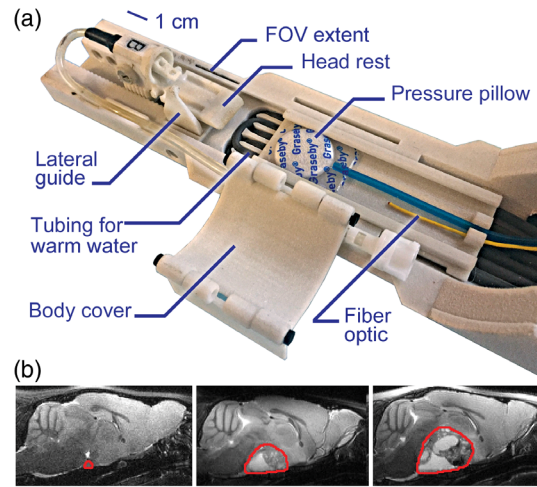

Fig. 7 (a) The mouse bed is 3D printed by selective laser sintering to provide sufficient detail. The bed features a side mark indicating the position of the field of view. The use of a hinged cover permitted to quickly secure or release the body of the animal. (b) MR images of the normal pituitary gland (highlighted in red) acquired during screening (left), and after the onset of cancer at different time points of tumor growth (center and right).

miniaturized mechanisms could be integrated into the RF coil fixture to adjust the resonant frequency or the impedance match.

The two coils ("coil 1" and "coil 2") were tested by measuring their quality factor. For coil 1, the quality factor was 705, and decreased to 370 when the coil was loaded with a mouse brain specimen. For coil 2, similar measurements gave an unloaded quality factor of 710 and a loaded quality factor of 380. This proved that the two coils were identical. In addition, the two coils were tested simultaneously during a DTI acquisition. Figure 7(c) shows that both coils acquired images with similar SNR and devoid of artifacts. Experimentally, the 3D-printed RF coil fixtures achieved an effective doubling of the DTI imaging throughput.[57]

3.5 Imaging Brain Tumors in Mice

In this application of brain tumor imaging in mice, 3D printing was used to increase the MR examination throughput so that a large number of animals could be studied as a single cohort. This was achieved by 3D printing a customized bed to expedite animal preparation, imaging, and shorten the overall duration of anesthesia in severely impaired animals.

Non-secreting pituitary adenomas, the most prevalent pituitary tumors in humans, develop spontaneously with age in mice genetically altered to carry a proopiomelanocortin null-mutant allele.[58] In this study, MRI was used to assess tumor onset, growth, and response to treatment with somatostatin/dopamine chimeric molecules. The study included 131 mice, screened weekly by MRI. Animals with a normal pituitary gland were re-enlisted for imaging the following week, whereas animals exhibiting a substantial pituitary gland neoplasm were enrolled in the subsequent phase of the MR study measuring adenoma volume at three different time points.

To handle the large animal cohort, a mouse bed was 3D printed to increase the throughput of each examination. The bed was equipped with a hinged body cover, allowing the mouse to be quickly secured on to the bed without taping the body or limbs, which in turn obviated the tedious removal

of adhesives from the rodent skin or fur after imaging. This saved several minutes from each preparation, allowing a more rapid turnaround between animals. Moreover, the 3D-printed bed featured a side mark to visually indicate the exact position of the imaging field of view. Hence, the mouse head could be correctly positioned before being moved to the center of the magnet. This rendered localizer scans and positional adjustments unnecessary, thereby saving another few minutes per animal. MR acquisition started directly with the screening protocol, which acquired eight sagittal slices, 400-μm thick, and placed 1 mm away from each other. If needed, volumetric MR measurement of the tumor size followed directly.

The bed reliably positioned the pituitary gland within the field of view of the screening protocol (20 mm × 14.4 mm × 10.2 mm) and within the larger imaging volume of the volumetric measurement scans. After scanning, the animal could be removed from the bed within seconds, and the next animal could be installed on the same bed and transported to the center of the magnet within a minute. This quick animal turnaround allowed isoflurane anesthesia to outlast imaging only by a few minutes, which was especially helpful during the care of late-stage, severely impaired, brain-tumor-bearing animals. Mice were scanned weekly, for up to 2 months, in a study that produced >1000 examinations under anesthesia, without any mortality during imaging.

4 Discussion

In vivo MR images were used directly to validate the different 3D-printed designs: the absence of motion artifacts demonstrated that the beds, dock, or RF coils achieved adequate immobilization of the organ of interest, in each imaging application. In addition, no shading was apparent in the *in vivo* MR images at the location of 3D-printed material, which indicated that the polylactide, engineered polymer, or resin that were used during the 3D-printing process were suitable to each application.

Beyond the processes described in this work, additive manufacturing has been used successfully to produce electronic and sensor circuits on nonplanar substrates.[59–62] Innovative 3D printers are able to expose a part to a controlled physical process after 3D printing. Each 3D-printing technique[63–68] achieves a different compromise between the electromechanical properties of the printed materials, the minimum or maximum size of the geometric features that can be produced, geometric complexity, surface finish, the amount of time required to print the part, the processing required after the deposition of materials, and the production cost.

While wireless transmission or flexible MRI coils have been demonstrated independently in MRI scanners,[69–71] these opportunities may permit the integration of preclinical RF coils, physiological monitoring sensors, and electronics into customized animal support beds. Such an integrated device could simplify animal handling, increase examination throughput, and potentially lower imaging cost.

5 Conclusion

3D printing offers rich opportunities to produce quickly and cost-effectively customized RF coils, MR-compatible apparatus, and fixtures simplifying animal handling and anesthesia. These opportunities can facilitate complex experiments, increase the consistency of MR data acquisition, and improve the throughput of small-animal MRI in specific applications, species or animals.

References

1. U. Steve and F. Richard, "The rapid prototyping technologies," *Assem. Autom.* **23**(4), 318–330 (2003).
2. D. H. Ballard et al., "Clinical applications of 3D printing: primer for radiologists," *Acad. Radiol.* **25**(1), 52–65 (2018).
3. K. Tappa and U. Jammalamadaka, "Novel biomaterials used in medical 3D printing techniques," *J. Funct. Biomater.* **9**(1), 17 (2018).
4. C.-Y. Liaw and M. Guvendiren, "Current and emerging applications of 3D printing in medicine," *Biofabrication* **9**(2), 024102 (2017).
5. D. Mitsouras et al., "Medical 3D printing for the radiologist," *Radiographics* **35**(7), 1965–1988 (2015).
6. B. Ripley et al., "3D printing from MRI data: harnessing strengths and minimizing weaknesses," *J. Magn. Reson. Imaging* **45**(3), 635–645 (2017).
7. M. Vukicevic et al., "Cardiac 3D printing and its future directions," *JACC Cardiovasc. Imaging* **10**(2), 171–184 (2017).
8. A. A. Giannopoulos et al., "Applications of 3D printing in cardiovascular diseases," *Nat. Rev. Cardiol.* **13**(12), 701–718 (2016).
9. C. H. A. Tam et al., "The role of three-dimensional printing in contemporary vascular and endovascular surgery: a systematic review," *Ann. Vasc. Surg.* **53**, 243–254 (2018).
10. A. A. Giannopoulos et al., "3D printed ventricular septal defect patch: a primer for the 2015 Radiological Society of North America (RSNA) hands-on course in 3D printing," *3D Print. Med.* **1**(1), 3 (2015).
11. E. L. Nyberg et al., "3D-printing technologies for craniofacial rehabilitation, reconstruction, and regeneration," *Ann. Biomed. Eng.* **45**(1), 45–57 (2017).
12. A. J. Bauermeister, A. Zuriarrain, and M. I. Newman, "Three-dimensional printing in plastic and reconstructive surgery a systematic review," *Ann. Plast. Surg.* **77**(5), 569–576 (2016).
13. J. L. Silberstein et al., "Physical models of renal malignancies using standard cross-sectional imaging and 3-dimensional printers: a pilot study," *Urology* **84**(2), 268–273 (2014).
14. H. H. Malik et al., "Three-dimensional printing in surgery: a review of current surgical applications," *J. Surg. Res.* **199**(2), 512–522 (2015).
15. F. Yang, V. Tadepalli, and B. J. Wiley, "3D printing of a double network hydrogel with a compression strength and elastic modulus greater than those of cartilage," *ACS Biomater. Sci. Eng.* **3**(5), 863–869 (2017).
16. S. Vijayavenkataraman et al., "3D bioprinting of tissues and organs for regenerative medicine," *Adv. Drug Delivery Rev.* **132**, 296–332 (2018).
17. S. V. Murphy and A. Atala, "3D bioprinting of tissues and organs," *Nat. Biotechnol.* **32**(8), 773–785 (2014).
18. C. Mandrycky et al., "3D bioprinting for engineering complex tissues," *Biotechnol. Adv.* **34**(4), 422–434 (2016).
19. Y. S. Zhang et al., "3D bioprinting for tissue and organ fabrication," *Ann. Biomed. Eng.* **45**(1), 148–163 (2017).
20. J. Norman et al., "A new chapter in pharmaceutical manufacturing: 3D-printed drug products," *Adv. Drug Delivery Rev.* **108**, 39–50 (2017).
21. H. Lauridsen et al., "From tissue to silicon to plastic: three-dimensional printing in comparative anatomy and physiology," *R. Soc. Open Sci.* **3**(3), 150643 (2016).
22. A. Goyanes et al., "PET/CT imaging of 3D printed devices in the gastrointestinal tract of rodents," *Int. J. Pharm.* **536**(1), 158–164 (2018).

23. F. Q. Wang et al., "Evaluation of an artificial vertebral body fabricated by a tantalum-coated porous titanium scaffold for lumbar vertebral defect repair in rabbits," *Sci. Rep.* **8**, 11 (2018).

24. C. Hoyer et al., "Advantages and challenges of small animal magnetic resonance imaging as a translational tool," *Neuropsychobiology* **69**(4), 187–201 (2014).

25. K. H. Herrmann et al., "3D printing of MRI compatible components: why every MRI research group should have a low-budget 3D printer," *Med. Eng. Phys.* **36**(10), 1373–1380 (2014).

26. K.-H. Herrmann et al., "MRI compatible small animal monitoring and trigger system for whole body scanners," *Z. Med. Phys.* **24**(1), 55–64 (2014).

27. B. Behzadnezhad et al., "Dielectric properties of 3D-printed materials for anatomy specific 3D-printed MRI coils," *J. Magn. Reson.* **289**, 113–121 (2018).

28. B. L. Cox et al., "An open source, 3D printed preclinical MRI phantom for repeated measures of contrast agents and reference standards," *Biomed. Phys. Eng. Express* **4**(2), 027005 (2018).

29. L. A. Dempsey et al., "Geometrically complex 3D-printed phantoms for diffuse optical imaging," *Biomed. Opt. Express* **8**(3), 1754–1762 (2017).

30. E. Doney et al., "3D printing of preclinical x-ray computed tomographic data sets," *JOVE J. Visualized Exp.* (73), e50250 (2013).

31. Z. P. Feng et al., "A rat model for pituitary stalk electric lesion-induced central diabetes insipidus: application of 3D printing and further outcome assessments," *Exp. Anim.* **67**(3), 383–392 (2018).

32. G. P. Howles et al., "Rapid production of specialized animal handling devices using computer-aided design and solid freeform fabrication," *J. Magn. Reson. Imaging* **30**(2), 466–471 (2009).

33. C. R. Lattin et al., "A 3D-printed modular device for imaging the brain of small birds," *J. Neurosci. Methods* **293**, 183–190 (2018).

34. R. E. McCarroll et al., "3D-printed small-animal immobilizer for use in preclinical radiotherapy," *J. Am. Assoc. Lab. Anim. Sci.* **54**(5), 545–548 (2015).

35. I. S. Negus et al., "Technical note: development of a 3D printed sub-resolution sandwich phantom for validation of brain SPECT analysis," *Med. Phys.* **43**(9), 5020–5027 (2016).

36. W. Neumann, L. R. Schad, and F. G. Zollner, "A novel 3D-printed mechanical actuator using centrifugal force for magnetic resonance elastography," in *39th Annu. Int. Conf. IEEE Eng. Med. and Biol. Soc.*, pp. 3541–3544 (2017).

37. R. M. Schoenfeld-Tacher et al., "Evaluation of 3D additively manufactured canine brain models for teaching veterinary neuroanatomy," *J. Vet. Med. Educ.* **44**(4), 612–619 (2017).

38. P. Stenroos et al., "Awake rat brain functional magnetic resonance imaging using standard radio frequency coils and a 3D printed restraint kit," *Front. Neurosci.* **12**, 548 (2018).

39. S. F. Wei et al., "Design and implementation of MRI RF coil based on 3D printing," in *IEEE MTT-S Int. Microwave Workshop Ser. RF and Wireless Technol. Biomed. and Healthcare Appl.*, pp. 222–224 (2015).

40. S. W. Yoon et al., "A precision 3D conformal treatment technique in rats: application to whole-brain radiotherapy with hippocampal avoidance," *Med. Phys.* **44**(11), 6008–6017 (2017).

41. H. Haug, "Brain sizes, surfaces, and neuronal sizes of the cortex cerebri—a strereological investigation of man and its variability and a comparison with some mammals (primates, whales, marsupials, insectivores, and one elephant)," *Am. J. Anat.* **180**(2), 126–142 (1987).

42. O. Beuf, F. Jaillon, and H. Saint-Jalmes, "Small-animal MRI: signal-to-noise ratio comparison at 7 and 1.5 T with multiple-animal acquisition strategies," *Magma* **19**(4), 202–208 (2006).

43. K. H. Herrmann et al., "Possibilities and limitations for high resolution small animal MRI on a clinical whole-body 3T scanner," *Magn. Reson. Mater. Phys. Biol. Med.* **25**(3), 233–244 (2012).

44. C. Baltes et al., "Micro MRI of the mouse brain using a novel 400 MHz cryogenic quadrature RF probe," *NMR Biomed.* **22**(8), 834–842 (2009).

45. K. R. Minard, R. A. Wind, and R. L. Phelps, "A compact respiratory-triggering device for routine microimaging of laboratory mice," *J. Magn. Reson. Imaging* **8**(6), 1343–1348 (1998).

46. S. K. Lemieux and G. H. Glover, "An infrared device for monitoring the respiration of small rodents during magnetic resonance imaging," *J. Magn. Reson. Imaging* **6**(3), 561–564 (1996).

47. S. Boretius et al., "MRI of cellular layers in mouse brain in vivo," *Neuroimage* **47**(4), 1252–1260 (2009).

48. D. Kokuryo et al., "A small animal holding fixture system with positional reproducibility for longitudinal multimodal imaging," *Phys. Med. Biol.* **55**(14), 4119–4130 (2010).

49. P. A. Flecknell, *Laboratory Animal Anaesthesia: An Introduction for Research Workers and Technicians*, Academic Press, London (1987).

50. I. C. Mundinano, P. A. Flecknell, and J. A. Bourne, "MRI-guided stereotaxic brain surgery in the infant and adult common marmoset," *Nat. Protocols* **11**(7), 1299–1308 (2016).

51. M. R. Bashir et al., "Emerging applications for ferumoxytol as a contrast agent in MRI," *J. Magn. Reson. Imaging* **41**(4), 884–898 (2015).

52. S. Svenningsen et al., "Hyperpolarized ^{3}He and ^{129}Xe MRI: differences in asthma before bronchodilation," *J. Magn. Reson. Imaging* **38**(6), 1521–1530 (2013).

53. R. S. Virgincar et al., "Quantitative analysis of hyperpolarized ^{129}Xe ventilation imaging in healthy volunteers and subjects with chronic obstructive pulmonary disease," *NMR Biomed.* **26**(4), 424–435 (2013).

54. J. M. Wang et al., "Using hyperpolarized ^{129}Xe MRI to quantify regional gas transfer in idiopathic pulmonary fibrosis," *Thorax* **73**(1), 21–28 (2018).

55. R. S. Virgincar et al., "A portable ventilator with integrated physiologic monitoring for hyperpolarized ^{129}Xe MRI in rodents," *J. Magn. Reson.* **295**, 63–71 (2018).

56. J. Schmiedeskamp et al., "Relaxation of spin polarized ^{3}He by magnetized ferromagnetic contaminants Part III," *Eur. Phys. J. D* **38**(3), 445–454 (2006).

57. J. Nouls et al., "Diffusion tensor imaging using multiple coils for mouse brain connectomics," *NMR Biomed.* **31**(6), e3921 (2018).

58. J. Karpac et al., "Proopiomelanocortin heterozygous and homozygous null mutant mice develop pituitary adenomas," *Cell Mol. Biol.* **52**, 135–140 (2006).

59. A. Kamyshny and S. Magdassi, "Conductive nanomaterials for printed electronics," *Small* **10**(17), 3515–3535 (2014).

60. D. Espalin et al., "3D printing multifunctionality: structures with electronics," *Int. J. Adv. Manuf. Technol.* **72**(5–8), 963–978 (2014).

61. Y. Y. Xu et al., "The boom in 3D-printed sensor technology," *Sensors* **17**(5), 1166 (2017).

62. Y. S. Rim et al., "Recent progress in materials and devices toward printable and flexible sensors," *Adv. Mater.* **28**(22), 4415–4440 (2016).

63. E. MacDonald and R. Wicker, "Multiprocess 3D printing for increasing component functionality," *Science* **353**(6307), aaf2093 (2016).

64. T. D. Ngo et al., "Additive manufacturing (3D printing): a review of materials, methods, applications and challenges," *Composites Part B* **143**, 172–196 (2018).

65. O. Oderinde et al., "Multifaceted polymeric materials in three-dimensional processing (3DP) technologies: current progress and prospects," *Polym. Adv. Technol.* **29**(6), 1586–1602 (2018).

66. C. Y. Yap et al., "Review of selective laser melting: materials and applications," *Appl. Phys. Rev.* **2**(4), 041101 (2015).

67. X. Wang et al., "3D printing of polymer matrix composites: a review and prospective," *Composites Part B* **110**, 442–458 (2017).

68. U. Ghosh et al., "Addressing unmet clinical needs with 3D printing technologies," *Adv. Healthcare Mater.* **7**(17), 1800417 (2018).

69. J. R. Corea et al., "Screen-printed flexible MRI receive coils," *Nat. Commun.* **7**, 10839 (2016).

70. S. B. Bulumulla et al., "Inductively coupled wireless RF coil arrays," *Magn. Reson. Imaging* **33**(3), 351–357 (2015).

71. J. Wei et al., "A realization of digital wireless transmission for MRI signals based on 802.11b," *J. Magn. Reson.* **186**(2), 358–363 (2007).

Biographies of the authors are not available.